

# CH<sub>3</sub>NH<sub>3</sub>PbI<sub>3</sub> Perovskites: Ferroelasticity Revealed

Evgheni Strelcov,<sup>1,2†</sup> Qingfeng Dong,<sup>3†</sup> Tao Li,<sup>4†</sup> Jungseok Chae,<sup>1,2†</sup> Yuchuan Shao,<sup>3,4</sup> Yehao Deng,<sup>3,4</sup> Alexei Gruveman,<sup>4\*</sup> Jinsong Huang,<sup>3\*</sup> and Andrea Centrone<sup>1\*</sup>

† These authors contributed equally to this work

\* Corresponding authors: AC [andrea.centrone@nist.gov](mailto:andrea.centrone@nist.gov), JH [jhuang2@unl.edu](mailto:jhuang2@unl.edu), AG [agruverman2@unl.edu](mailto:agruverman2@unl.edu)

<sup>1</sup> Center for Nanoscale Science and Technology, National Institute of Standards and Technology  
100 Bureau Drive, Gaithersburg, MD 20899, USA.

<sup>2</sup> Maryland Nanocenter, University of Maryland, College Park, MD 20742 USA.

<sup>3</sup> Department of Mechanical and Materials Engineering, University of Nebraska-Lincoln,  
Lincoln, Nebraska 68588, USA.

<sup>4</sup> Department of Physics and Astronomy, University of Nebraska-Lincoln, Lincoln, Nebraska  
68588, USA

## Abstract

Ferroelectricity has been proposed as a plausible mechanism to explain the high photovoltaic conversion efficiency in organic-inorganic perovskites; however, convincing experimental evidence in support of this hypothesis is still missing. Identifying and distinguishing ferroelectricity from other properties such as piezoelectricity, ferroelasticity, etc., is typically non trivial because these phenomena can coexist in many materials. In this work, a combination of microscopic and nanoscale techniques provides solid evidence for the existence of ferroelastic domains in both CH<sub>3</sub>NH<sub>3</sub>PbI<sub>3</sub> polycrystalline films and single crystals in the pristine state and under applied stress. Experiments show that the configuration of CH<sub>3</sub>NH<sub>3</sub>PbI<sub>3</sub> ferroelastic domains

in single crystals and polycrystalline films can be controlled with applied stress suggesting that strain engineering may be used to tune the properties of this material. No evidence of concomitant ferroelectricity was observed. Because grain boundaries have an impact on the long term stability of organic-inorganic perovskites devices, and because the ferroelastic domain boundaries may differ from regular grain boundaries, the discovery of ferroelasticity provides a new variable to consider in the quest for improving their stability and enabling their widespread adoption.

## **Introduction**

In the past few years, organic-inorganic perovskite (OIP) materials have drawn significant attention driven by their potential for realizing the next generation of low-cost and high efficiency solar cells (1-4). The power conversion efficiency (PCE) of small-size (typically  $< 16 \text{ mm}^2$ ) perovskite solar cells improved considerably, from 3.9 % in 2009 to 22.1 % in 2016 (5, 6). Perhaps even more remarkably, the PCE of large devices ( $> 1 \text{ cm}^2$ ) has rapidly approached 20 % (7). This extraordinary performance benefits from the unusual combination of properties of OIPs, such as strong optical absorption, small exciton binding energy, high carrier mobility, long charge carrier life time, long charge diffusion length, and small density of deep traps in spite of the large point defect densities typical of solution processed films (8, 9). However, the pace of knowledge gathering on OIPs fundamental properties, has in general lagged far behind the pace of efficiency improvement. For example, the widespread observation of current hysteresis in OIP devices, and the recent observation of the switchable diode and photovoltaic effects, initially spurred the speculation that OIPs could be ferroelectric at room temperature (10-15). This hypothesis prompted the fascinating idea that an internal field due to spontaneous polarization might be at the origin of the high PCE in OIP solar cells by aiding separation of photoexcited electron-hole pairs,

and thus reducing charge recombination (16). However, solid experimental evidence of ferroelectricity of OIP materials is still lacking and recent publications (17, 18) even question the very polarity of the  $\text{CH}_3\text{NH}_3\text{PbI}_3$  ( $\text{MAPbI}_3$ ) structure, a necessary requirement for ferroelectricity. Additionally, several recent studies conclusively showed that ion migration and the associated charge doping are responsible for the observed hysteretic effects and excluded ferroelectricity as possible origin (19). Domain-like structures have been recently observed by piezoresponse force microscopy (PFM) imaging (20), but no reproducible evidence for polarization-electric field hysteresis loops (the “smoking gun” for ferroelectricity) have been provided for either thin film or single crystal  $\text{MAPbI}_3$  devices. Hermes et al. (20) have proposed that the domain-like structures consist of twin domains that form in  $\text{CH}_3\text{NH}_3\text{PbI}_3$  during the cubic-tetragonal phase transition due to strain, thus indicating a ferroelastic, rather than ferroelectric behavior. However, these claims still lack the conclusive support of macroscopic and strain-related evidence.

In this work, a combination of microscopic (polarized-light optical microscopy) and nanoscopic (piezoresponse force microscopy and photothermal induced resonance) characterization techniques provide solid evidence for the ferroelastic behavior of  $\text{CH}_3\text{NH}_3\text{PbI}_3$ . This conclusion is supported by measurements of  $\text{CH}_3\text{NH}_3\text{PbI}_3$  in the pristine state and under applied stress and electrical bias. Ferroelastic behavior of micro- and nanoscopic domains was observed both in  $\text{CH}_3\text{NH}_3\text{PbI}_3$  polycrystalline samples and single crystals as a function of the applied stress. Because grain size and grain boundaries are important factors influencing the long term stability of OIP devices – one of the most important issues hindering their widespread adoption – the results presented here could have important implications for their practical application.

## Results

Akin to ferroelectricity and to ferromagnetism, for which multiple orientation states can coexist in a crystal at zero electric and magnetic field, respectively, ferroelasticity occurs when spontaneous strain enables the coexistence of different orientation states in a crystal, which can be switched from one state to another by external stress (21, 22). The ferroelastic orientation state in a material is determined by its unique spontaneous strain tensor, similarly to how spontaneous polarization leads to ferroelectricity. According to the available data, (17) MAPbI<sub>3</sub> exists in 3 crystallographic phases: cubic ( $Pm\bar{3}m$ ), above 327 K, tetragonal ( $I4/mcm$ ) between 327 K and 162 K, and orthorhombic ( $Pnma$ ) below 162 K. The cubic-tetragonal transition, that lowers the symmetry from the  $m\bar{3}m$  to the  $4/mmm$  centrosymmetric point group, is a purely ferroelastic transition according to the Aizu's classification (i.e. the resulting tetragonal phase can be ferroelastic but not ferroelectric) (23, 24).

Three different types of samples were fabricated using three different established methods: two-step spin-coating (25) (*Sample A1*, *Sample A2*) followed by thermal annealing, doctor blading (26), (*Sample B1 and B2*) with *in situ* annealing, and inverse temperature crystallization single crystal growth (27) (*Sample C*). Spin coating and doctor blading yielded polycrystalline films with grain sizes (areas) ranging from 0.25  $\mu\text{m}^2$  to 4  $\mu\text{m}^2$ . *Sample A1* was deposited on Poly[bis(4-phenyl)(2,4,6-trimethylphenyl)amine] (PTAA) coated indium tin oxide (ITO) substrates, *Sample A2* was spin coated on a zinc sulphide optical prism to enable characterization with the photothermal induced resonance (PTIR) technique. *Sample B1* has a thickness of  $\approx 600$  nm and was deposited on a flexible polyethylene terephthalate substrate to study stress induced changes of OIP ferroelastic domains. *Sample B2* was deposited on a rigid ITO substrate to study the effect of the electrical bias on the domain structures. The recently developed single crystal growth

method yielded a very thin single crystal with lateral dimensions of 2 mm × 5 mm and thickness of 20 μm (*Sample C*). Details of sample fabrication can be found in the experimental section.

To investigate the ferroelastic properties and to demonstrate control of the ferroelastic state in MAPbI<sub>3</sub>, we synthesized a large and thin (20 μm) single crystal (*Sample C*) with ferroelastic domains wide enough to i) be measured in situ with optical microscopy and ii) to enable the application of stress macroscopically. The co-existence of multiple orientation states within a crystal necessarily requires the formation of domain boundaries, for which the energetics in relation to external fields are well described by the Ginzburg–Landau formalism (28, 29). Symmetry determines which domain boundaries are permissible. The MAPbI<sub>3</sub> cubic to tetragonal transition divides a crystal into a system of tetragonal twins (ferroelastic domains) whose orientation on average must retain the higher symmetry of the prototypical cubic phase. The transition from the cubic  $Pm\bar{3}m$  phase to the  $I4/mcm$  tetragonal phase ( $m3mF4/mmm$  transition according to Aizu) (23) can produce 6 types of domain orientations, (22) hereafter referred as ZY, Z-Y, ZX, Z-X, XY, -XY (see Fig. 1D). Importantly, such domain orientations are characterized by domain walls intersecting at 0°, 90° or 45° in the principal plains of the crystal (i.e. 001, 100, 010 families) but they may also intersect at about 70° and 110° in other planes (e.g. the (110) plane).

Polarized-light optical microscopy is a simple, yet effective, method to study the ferroelastic materials (30). Because the refractive index is a directional property in anisotropic crystals, the intensity of light transmitted through or reflected by such crystals depends on the relative orientation of the principal optical axes with respect to the direction of the linear polarization of incident light. Interaction with the crystal rotates the light polarization direction, which is typically detected by passing the light through an analyzer with polarization perpendicular to the

polarization of the incident light. Polarized light microscopy images (Fig. 1A to C) show domains within the large MAPbI<sub>3</sub> crystal. The bright domains correspond to the reflected light with the polarization plane parallel to the analyzer. Sample rotation relative to the polarizer-analyzer pair identifies the extinction angle ( $\theta_e$ , the angle at which a group of domains becomes extinct). An additional sample rotation through  $\theta_e/2$  degrees makes the domain groups indistinguishable leaving only domain walls faintly visible (Fig. 1B). Based on Fig. 1,  $\theta_e$  was 90°, as expected for the tetragonal phase.

*Sample C* was glued to a flexible substrate, which was bent upward or downward to create tensile or compressive strain in the crystal, respectively. The evolution of the domain structure in the MAPbI<sub>3</sub> crystal under stress, an inherent feature of ferroelastic materials, is reported in Fig. 2. We have chosen the domain group area fraction ( $F$ ) with respect to the whole field of view to be a relevant descriptor of the sample behavior:  $F = \frac{Area_{bright} - Area_{dark}}{Area_{bright} + Area_{dark}}$ . Thus,  $F = 1$  (-1) implies that all of the field of view is filled with a bright (dark) single domain and  $F = 0$  implies equal areas for dark and bright domains. Fig. 2 shows the domain area fraction vs. stress plot together with optical images at selected points of the stress cycle (points A to H). Although the  $F$  vs. stress plot has a complex shape and differs from the classic strain-stress hysteresis curve, (21) (note that its relationship with strain is non-trivial(31)) it represents well and consolidates the rich data displayed by multiple images (Fig 2). Starting with an approximately equal domain population (Fig. 2A,  $F \approx 0$ ), the system evolved into a state with predominantly bright domains under tensile stress ( $F$  increases). The most important observation is that a new family of bright domains with walls tilted 70° and 109° with respect to the old domains appears in response to the application of a large tensile stress (Fig. 2B). The formation of these domains is associated with a minimum in the domain area fraction (at stress  $\approx 0.5$  a.u.). Consequently, the preceding  $F$  maximum (at stress =

0.3 a.u.) must arise due to minimization of system's energy in the wake of transition that yields the  $70^\circ$ -domains. Releasing the stress gradually reduces the density of the new domains (reflecting a decrease of the elastic energy stored in the material) until their disappearance (Fig. 2B to E) and yields a negative  $F$  (Fig. 2C to F). Upon a further increase of the compressive stress, the system undergoes a sharp transition characterized by the complete disappearance of bright domains (Fig. 2F to G). Beyond this point the crystal yielded, cracking and relieving some of the strain. The nearly-zero stress domain pattern re-appeared (Fig. 2H) and system became only weakly responsive to the applied stress afterwards. The plot is clearly hysteretic and non-linear, as typical for ferroelastic materials, and indicates that the domains in *Sample C* are: a) affected by external stress, b) exist at nominally zero stress, c) do not return to the same state upon stress cycling, i.e. revealing the hysteretic nature of material's response to the applied stress.

The appearance of the  $70^\circ$  domain walls is unusual for a tetragonal crystal. Twins in  $\text{SrTiO}_3$ (32) and  $\text{KMnF}_3$ (33) ( $I4/mcm$  group), for example, show only  $0^\circ$ ,  $45^\circ$  and  $90^\circ$  domain walls. This apparent discrepancy allows estimating the crystal orientation, which could not be measured directly by electron backscattered diffraction, due to electron irradiation damage to the material. Indeed, although  $70^\circ$  domain walls are not permitted for the principal planes, they are possible for the (110) plane (see Fig. 2D). By comparing the domain schematic in Fig. 2D with Fig. 2B, C and D, we conclude that the wide bright and dark domains in Fig. 2 could be identified as Z and -Y, whereas the needle-like bright domains that grow from the left under tensile stress could be identified as X domains according to the classification introduced earlier, suggesting that the top plane of our sample should be (110). Interestingly, Hermes et al.(20) observed only  $0^\circ$  and  $90^\circ$  domain walls in the (110)  $\text{MAPbI}_3$  plane, presumably, because they did not strain their sample enough to induce the formation of X domains. X-ray micro-diffraction measurements would be

necessary to unambiguously identify the crystallographic orientation of the sample and the nature of its domains.

Next, we provide evidence of ferroelasticity and intra-grain strain in perovskite thin films (with small grains) using piezoresponse force microscopy (PFM) (34, 35). PFM enables detection of the electrically-induced mechanical response of a sample. To avoid sample degradation, the PFM measurements were performed in a nitrogen environment. While stripe domains were observed in both samples, *Sample B1* always shows higher stripe density than *Sample A1*. Stripe domains are not observed in all grains of *Sample A1* and the stripe orientation differs among adjacent grains (Fig. S1D). The doctor-blading process was conducted at a significantly higher temperature (145 °C) than spin coating (105 °C). Consequently, it is reasonable to expect that *Sample A1* may have smaller internal stress than *Sample B1*, driven by the difference of the thermal expansion coefficients between the perovskite and the substrate and the temperature difference with respect to ambient conditions. Of course, other factors such as film crystallization temperature and the substrate material may also be important. *Sample B1* (Fig. 3B) also shows that the orientation of two groups of stripes within a grain intersects at  $\approx 70^\circ$ , which is consistent with the domain configuration described in Fig. 1D.

To examine whether the ferroelastic twin domains can be switched by external stress applied locally, we gradually increased the force exerted by the PFM tip while scanning the area enclosed by the white dashed square in Fig. 3D. The loading force is controlled and maintained by a typical feedback loop of contact mode AFM. We observed that a 200 nN loading force was sufficient to damage the surface of the perovskite film, making the direct observation of ferroelastic domain switching with the force supplied locally by the PFM tip challenging. Hence, to demonstrate the stress-tunability of the ferroelastic domains we performed PFM imaging using

a low loading force ( $< 40$  nN) before, during and after application of a macroscopic stress to the OIP film by bending the film (2 cm bending radius). Fig. 4A and B show the morphology and corresponding ferroelastic domains in the pristine state (no external stress). Under tensile stress (Fig. 4C and D), the narrow stripes coalesced, forming wider stripes, and the dark purple domains disappeared. After relieving the stress, the domain pattern did not return to the original state and the ratio between light and dark domains changed (Fig. 4E and F). The height images obtained before and after stressing the sample appear unaltered, except for the sharp ridges that are smoothed in the latter. In contrast to the PFM amplitude images, the PFM phase images show only very weak contrast at the ferroelastic domain boundaries (see representative phase image in Fig. S2C). Strong and weak contrast in the amplitude and phase PFM images, respectively, can be considered as a strong indicator that the sample may not be a ferroelectric (10).

To further test whether the ferroelastic domains could also display ferroelectricity, *Sample B2* was investigated with PFM by sweeping the applied bias with the tip at specific locations and on a larger scale by measuring PFM images under applied bias (Fig. S1). However, no change of the phase signal (Fig. S1A) was observed following the local sweep of the DC bias ( $\pm 2.5$  V). It is likely that the applied DC bias may not be sufficient to switch the polarization of the film that is hundreds of nanometers thick. Application of DC bias ( $\pm 2$  V) to *Sample A1* also did not induce any significant contrast changes in the PFM phase image (Fig. S1F to H). The local ion concentration may also be altered by the DC bias and affect the strength of the piezoresponse. Thus no conclusion regarding the ferroelectric properties of the sample can be made based on the obtained data.

To further characterize the domains at the nanoscale and to investigate *in situ* whether they are susceptible to electrical bias, we used the photothermal induced resonance (PTIR) technique (36,

37). PTIR is a novel method that combines the lateral resolution of AFM with the specificity of absorption spectroscopy. PTIR was initially developed in the mid-IR, (36) and has attracted much interest for enabling label-free composition mapping, (38-41) material identification (42) and conformational analysis (43, 44) at the nanoscale. For example, PTIR data yielded direct evidence of MA<sup>+</sup> electro-migration and in OIP lateral structure solar cells (39). Very recently, we extended PTIR to the visible and near-IR spectral ranges (45); an advance that has enabled the determination of the local bandgap in CH<sub>3</sub>NH<sub>3</sub>PbI<sub>3-x</sub>Cl<sub>x</sub> films and estimating the local Cl<sup>-</sup> content as a function of the annealing process (46). In our PTIR set up a pulsed wavelength-tunable laser (spot size  $\approx$  30  $\mu$ m) is used to illuminate the sample via total internal reflection (Fig. 5A). An AFM tip contacting the sample locally transduces the thermal expansion of the sample due to light absorption, into cantilever oscillations that are monitored by the AFM 4-quadrant detector. The amplitude of the cantilever oscillation (PTIR signal) is proportional to the absorbed energy (47, 48) and yields nanoscale absorption spectra (vibrational or electronic) when sweeping the laser wavelength while holding the tip at a given location. Alternatively, PTIR absorption maps are obtained illuminating the sample at a given wavelength at a time and by plotting the PTIR signal as a function of the tip position. To enable PTIR characterization at both mid-IR and visible ranges, a polycrystalline OIP lateral device was fabricated on the surface of a zinc sulfide prism by spin coating (*Sample A2*; see experimental for details). Here we show that the PTIR transduction scheme enables the visualization of ferroelastic domains thanks to their orientation dependent anisotropic thermal expansion coefficient.

Fig. 5B shows the topography of the OIP layer in the area between the device electrodes (See Fig. S3 of the supporting information for a larger field of view). Interestingly, the PTIR maps obtained by illuminating the sample at 1468 cm<sup>-1</sup> (6.81  $\mu$ m) corresponding to the CH<sub>3</sub> asymmetric

deformation of the methylammonium ion (Fig. 2C) and  $13250\text{ cm}^{-1}$  ( $1.64\text{ eV}$ ,  $\approx 755\text{ nm}$ , Fig. 2D) corresponding to electronic excitation just above the bandgap, show stripe domains on most grains. The width of the domains ranges from  $100\text{ nm}$  to  $225\text{ nm}$ . In previous work, (49) we identified one grain in a  $\text{MAPbI}_3$  film showing similar striations which were tentatively related to the beginning of the perovskite decomposition process during high temperature annealing. Here, we argue that such striations should be ascribed to the presence of ferroelastic domains instead. Fig. 5E shows representative PTIR spectra measured from two adjacent striations. Previously, Chae *et al* (46) showed that local bandgap value in  $\text{CH}_3\text{NH}_3\text{PbI}_{3-x}\text{Cl}_x$  correlates with the  $\text{Cl}^-$  content ( $x$ ) and decreases upon annealing. By linearly fitting the electronic spectra absorption profile we derive an optical bandgap of  $1.57\text{ eV} \pm 0.10\text{ eV}$  suggesting a negligible  $\text{Cl}^-$  content (i.e.  $x \approx 0$ ). Throughout the manuscript, the uncertainty of the bandgap represents a single standard deviation in the linear fitting of the PTIR absorption spectra. The PTIR spectra of contiguous domains share the same spectral characteristics i.e. differ only in intensity, but not in peak position or optical bandgap, suggesting that the spectral differences arise from structural factors such as crystal orientation or crystal anisotropy rather than from composition variations. Typically, the intensity of vibrational excitations in crystals depends on the relative orientation between linearly polarized incident light and the crystal dipole moment. However, polarization dependent PTIR maps (Fig. S4) show that the striation patterns and their relative intensities for all crystals are the same with both s-polarization (in the sample plane) and p-polarization (polarization components in and out of the sample plane) excitation. This is not surprising because the  $\text{MA}^+$  exhibits fast rotational dynamics within the perovskite inorganic framework (50). Because the sample thermal expansion coefficient in the vertical direction modulates the PTIR signal amplitude, (38, 48) the differences in the PTIR intensity are attributed to differences in the local thermal expansion coefficient ( $\alpha$ )

which in MAPbI<sub>3</sub> is larger along the *a* axis ( $\alpha_a = 1.32 \times 10^{-4} \text{ m/m}^{-1}\cdot\text{K}^{-1}$ ) than along the *c* axis ( $\alpha_c = -1.06 \times 10^{-4} \text{ m/m}^{-1}\cdot\text{K}^{-1}$ ) (51). The observation of the same exact striation patterns in the PTIR images corresponding to both vibrational absorption (Fig. 5C) and electronic absorption (Fig. 5D) further support this interpretation. In other words, the striations result from differences in thermo-mechanical transduction rather than from optical absorption (i.e. composition variations). Because the ferroelastic twinning that takes place during the cubic-tetragonal phase transition occurs independently in each grain, the ferroelastic domain patterns (striations) are unique to each grain.

Hermes *et al* (20) provided evidence of ferroelastic domains in MAPbI<sub>3</sub> but could not provide evidence of concomitant ferroelectricity. However, the authors argued that the absence of polarization switching under a tip-applied bias in their samples was not sufficient to definitely exclude ferroelectricity because the vertically applied field may not be effective in switching domains with in-plane polarization components (20). To test that possibility the lateral device structure in *Sample A2* was leveraged to apply an electric field (up to  $1 \text{ V}\cdot\mu\text{m}^{-1}$ ) in the sample plane. The AFM topography images (Fig. 5F) and the PTIR maps (Fig. 5G and H) obtained after applying a  $0.86 \text{ V}\cdot\mu\text{m}^{-1}$  lateral electric field for 1 minute do not show any differences with respect to the topographic and PTIR images of the same area obtained before electrical poling (Fig. 5B to D). In summary, in all our tests we do not observe evidence of electrical polarization switching of the domain structure. No change in topography and in the PTIR maps was observed with up to  $1 \text{ V}\cdot\mu\text{m}^{-1}$  applied electric field.

## Discussion

In conclusion, different nanoscale and microscopic techniques provide solid evidence of ferroelasticity in both MAPbI<sub>3</sub> polycrystalline films and single crystals that were obtained with different fabrication methods. No evidence of concomitant ferroelectricity was observed for the experimental conditions and materials studied here. We show that the configuration of MAPbI<sub>3</sub> ferroelastic domains in OIPs can be controlled with applied stress and we propose strain engineering as a new lever to control the optoelectronic properties of OIP devices. Because poor long term stability is an obstacle for the deployment of OIP devices on a large scale, and because grain boundaries are an important factor for determining the stability of such devices, our results could have considerable implications for their practical application. In fact, OIP grain sizes are typically determined based on SEM or AFM topographic images, which may or may not reflect the internal grain structure appropriately. Additionally, more and more observations suggest that OIP with nominally identical composition may display significantly different thermal or chemical stability, thus it will be important to understand if differences in the grain structure are related to grain stability. It is possible that the single crystals and polycrystals reported in the literature may consist of ferroelastic twin domains. We believe that our observations will foster studies aimed at determining the role of ferroelastic domains and strain engineering to improve the OIP chemical and thermal stability and photovoltaic performance.

## **Materials and Methods**

*Sample preparation:* Two-step spin-coating of perovskite polycrystalline films: *Sample A1* was fabricated using the procedure described in our previous work (25). *Sample A2* was prepared by a multicycle spin-coating process described in our previous work (52).

Doctor blade coating of perovskite polycrystalline films: films were fabricated using a modification of the procedure used in our previous work (26). The perovskite precursor solution (MAPbI<sub>3</sub>/DMSO, 1 mol/L) was doctor blade coated on a UV-ozone treated ITO substrate at room temperature and heated at 145 °C in a semi-enclosed chamber for 5 min yielding a crystalline perovskite film. Subsequently, the film was annealed *in situ* at 100 °C for 30 min to remove the solvent. The single crystal was grown by using inverse temperature crystallization (27).

*Polarized-light optical microscopy:* was performed in reflection mode in the cross Nicols configuration on a commercially available microscope. For the stress measurements a MAPbI<sub>3</sub> crystal (about 2 mm × 5 mm × 20 μm in size) was attached with a polyimide adhesive tape to a stainless steel plate (17.2 mm × 12.5 mm × 0.22 mm). The plate was placed between the jaws of a miniature vice in a glove bag under the microscope. The generated stress was proportional to the plate buckling. The domain fraction  $F$  was calculated as:  $F = \frac{Area_{bright} - Area_{dark}}{Area_{bright} + Area_{dark}}$ . Uncertainty in  $F$  was calculated as the ratio of the sum of uncertainties of each domain boundary (domain boundary area) to the total area of the image for a few representative points: A (0.016), E (0.020), F (0.018), and last two points on the graph close to zero stress (0.030 and 0.029).

*Piezoresponse Force Microscopy measurements:* A commercial AFM was used to perform the PFM measurements. The MAPbI<sub>3</sub> films were characterized in a small closed cell with continuous dry nitrogen flow to prevent film degradation. The films were grounded through the ITO layer. An AC bias with an amplitude of 1 V was applied to the film via a Pt/Ir-coated Si tip. A resonance enhancement mode (Dual AC Resonance Tracking) was used to amplify the piezoresponse signal (53). The typical drive frequency was in the range between 320 kHz to 360 kHz depending on the

contact resonant frequency. The typical loading force for PFM scan was in the range from 20 nN to 40 nN, which did not damage the film surface during the PFM imaging.

To measure the piezoresponse on the MAPbI<sub>3</sub> film that was macroscopically deformed, the film along with the flexible substrate was fixed on a customized rigid plastic bridge with radius of curvature of 20 mm using double-sided tape. The central region of the MAPbI<sub>3</sub> film where the maximum tensile stress occurs was studied using PFM. The same location was traced and scanned before, during, and after the stress application.

The switching spectroscopy-PFM (SS-PFM) technique was used to acquire the hysteresis loops from the MAPbI<sub>3</sub> film. A typical triangle-square DC wave with AC bias was applied (54). The off state data (i.e. when DC bias = 0) was used to plot the hysteresis loops. The amplitude loop reveals the strain hysteresis, while the phase loop demonstrates the polarization switching process if it exists.

*PTIR characterization:* PTIR experiments were carried out in nitrogen atmosphere using a modified commercial PTIR setup that consists of an AFM microscope operating in contact mode and 3 tunable pulsed laser sources (laser A, B, C) which have been described previously (40, 45). Two of the three laser sources (Laser A and Laser C) were used in this work. Laser A consists of a Q-switched diode pumped Nd:YAG laser (1064 nm), one optical parametric oscillator (OPO) based on a periodically poled lithium niobate (PPLN) crystal and a second OPO based on a non-critically phase-matched ZnGeP<sub>2</sub> (ZGP) crystal. Laser A emits 10 ns pulses that are tunable from 4000 cm<sup>-1</sup> to  $\approx$  1025 cm<sup>-1</sup> (from 2.5  $\mu$ m to 9.76  $\mu$ m) at 1 kHz repetition rate and with line widths between 5 cm<sup>-1</sup> and 16 cm<sup>-1</sup> depending on the wavelength. Laser C consists of a nanosecond Q-switched diode pumped Nd:YAG pump laser and an OPO based on a beta barium borate non-

linear crystal integrated into a single enclosure. Laser C emits 10 ns pulses with  $< 1$  nm line width at 1 KHz repetition rate in the range from 400 nm to 2300 nm. The low repetition rate of the laser assures that a new pulse will excite a sample and cantilever after they have returned to equilibrium. The typical laser spot size is  $\approx 30$   $\mu\text{m}$  at the sample. PTIR experiments were obtained by flowing nitrogen gas ( $0.12 \text{ dm}^3 \cdot \text{s}^{-1}$ ) in custom enclosure built around the sample.

MAPbI<sub>3</sub> samples for PTIR analysis were fabricated according to the procedure described above directly on a zinc sulphide right angle prism with Au electrodes fabricated by photo lithography and lift-off technique, using a custom spinner adaptor. A voltage source unit was used for electrical poling *Sample A2* by applying a maximum of 7 V between two Au electrodes (spaced by 7  $\mu\text{m}$ ).

PTIR spectra were obtained by averaging the cantilever deflection amplitude from 256 individual laser pulses at each wavelength and tuning the laser at intervals of 4  $\text{cm}^{-1}$  and 50  $\text{cm}^{-1}$  for laser A and C, respectively. PTIR images were recorded by illuminating the sample with a constant wavelength while scanning the AFM tip. The AFM height and the PTIR signal acquisition was synchronized so that for each AFM pixel the PTIR signal is an average over 32 laser pulses. The pixel sizes are 20 nm  $\times$  20 nm for Fig. 4 and 50 nm  $\times$  50 nm for all images in supplemental information. Commercially available 450  $\mu\text{m}$  long silicon contact-mode AFM probes with a nominal spring constant between 0.07 N/m and 0.4 N/m were used.

## References:

1. M. A. Green, A. Ho-Baillie, H. J. Snaith, The emergence of perovskite solar cells. *Nature Photonics* **8**, 506-514 (2014).
2. J. H. Heo, S. H. Im, J. H. Noh, T. N. Mandal, C. S. Lim, J. A. Chang, Y. H. Lee, H. J. Kim, A. Sarkar, M. K. Nazeeruddin, M. Gratzel, S. I. Seok, Efficient inorganic-organic hybrid

- heterojunction solar cells containing perovskite compound and polymeric hole conductors. *Nature Photonics* **7**, 487-492 (2013).
3. M. M. Lee, J. Teuscher, T. Miyasaka, T. N. Murakami, H. J. Snaith, Efficient Hybrid Solar Cells Based on Meso-Superstructured Organometal Halide Perovskites. *Science* **338**, 643-647 (2012).
  4. H. J. Snaith, Perovskites: The Emergence of a New Era for Low-Cost, High-Efficiency Solar Cells. *Journal of Physical Chemistry Letters* **4**, 3623-3630 (2013).
  5. A. Kojima, K. Teshima, Y. Shirai, T. Miyasaka, Organometal Halide Perovskites as Visible-Light Sensitizers for Photovoltaic Cells. *Journal of the American Chemical Society* **131**, 6050-+ (2009).
  6. [http://www.nrel.gov/ncpv/images/efficiency\\_chart.jpg](http://www.nrel.gov/ncpv/images/efficiency_chart.jpg).
  7. X. Li, D. Q. Bi, C. Y. Yi, J. D. Decoppet, J. S. Luo, S. M. Zakeeruddin, A. Hagfeldt, M. Gratzel, A vacuum flash-assisted solution process for high-efficiency large-area perovskite solar cells. *Science* **353**, 58-62 (2016).
  8. S. D. Stranks, G. E. Eperon, G. Grancini, C. Menelaou, M. J. Alcocer, T. Leijtens, L. M. Herz, A. Petrozza, H. J. Snaith, Electron-Hole Diffusion Lengths Exceeding 1 Micrometer in an Organometal Trihalide Perovskite Absorber. *Science* **342**, 341-344 (2013).
  9. Q. Dong, Y. Fang, Y. Shao, P. Mulligan, J. Qiu, L. Cao, J. Huang, Electron-hole diffusion lengths > 175  $\mu\text{m}$  in solution-grown  $\text{CH}_3\text{NH}_3\text{PbI}_3$  single crystals. *Science* **347**, 967-970 (2015).
  10. Z. G. Xiao, Y. B. Yuan, Y. C. Shao, Q. Wang, Q. F. Dong, C. Bi, P. Sharma, A. Gruverman, J. S. Huang, Giant switchable photovoltaic effect in organometal trihalide perovskite devices. *Nature Materials* **14**, 193-198 (2015).
  11. H. J. Snaith, A. Abate, J. M. Ball, G. E. Eperon, T. Leijtens, N. K. Noel, S. D. Stranks, J. T. W. Wang, K. Wojciechowski, W. Zhang, Anomalous Hysteresis in Perovskite Solar Cells. *Journal of Physical Chemistry Letters* **5**, 1511-1515 (2014).
  12. J. M. Frost, K. T. Butler, A. Walsh, Molecular ferroelectric contributions to anomalous hysteresis in hybrid perovskite solar cells. *APL Materials* **2**, 081506 (2014).
  13. H. W. Chen, N. Sakai, M. Ikegami, T. Miyasaka, Emergence of Hysteresis and Transient Ferroelectric Response in Organo-Lead Halide Perovskite Solar Cells. *Journal of Physical Chemistry Letters* **6**, 164-169 (2015).
  14. B. Chen, X. Zheng, M. Yang, Y. Zhou, S. Kundu, J. Shi, K. Zhu, S. Priya, Interface band structure engineering by ferroelectric polarization in perovskite solar cells. *Nano Energy* **13**, 582-591 (2015).
  15. J. Wei, Y. C. Zhao, H. Li, G. B. Li, J. L. Pan, D. S. Xu, Q. Zhao, D. P. Yu, Hysteresis Analysis Based on the Ferroelectric Effect in Hybrid Perovskite Solar Cells. *Journal of Physical Chemistry Letters* **5**, 3937-3945 (2014).
  16. J. M. Frost, K. T. Butler, F. Brivio, C. H. Hendon, M. van Schilfgaarde, A. Walsh, Atomistic origins of high-performance in hybrid halide perovskite solar cells. *Nano letters* **14**, 2584-2590 (2014).
  17. G. Sharada, P. Mahale, B. P. Kore, S. Mukherjee, M. S. Pavan, C. D. De, S. Ghara, A. Sundaresan, A. Pandey, T. N. G. Row, D. D. Sarma, Is  $\text{CH}_3\text{NH}_3\text{PbI}_3$  Polar? *Journal of Physical Chemistry Letters* **7**, 2412-2419 (2016).

18. Y. Dang, Y. Liu, Y. Sun, D. Yuan, X. Liu, W. Lu, G. Liu, H. Xia, X. Tao, Bulk crystal growth of hybrid perovskite material  $\text{CH}_3\text{NH}_3\text{PbI}_3$ . *CrystEngComm* **17**, 665-670 (2015).
19. J. Beilsten-Edmands, G. E. Eperon, R. D. Johnson, H. J. Snaith, P. G. Radaelli, Non-ferroelectric nature of the conductance hysteresis in  $\text{CH}_3\text{NH}_3\text{PbI}_3$  perovskite-based photovoltaic devices. *Applied Physics Letters* **106**, (2015).
20. I. M. Hermes, S. A. Bretschneider, V. W. Bergmann, D. Li, A. Klasen, J. Mars, W. Tremel, F. Laquai, H.-J. Butt, M. Mezger, R. Berger, B. J. Rodriguez, S. A. L. Weber, Ferroelastic Fingerprints in Methylammonium Lead Iodide Perovskite. *The Journal of Physical Chemistry C* **120**, 5724-5731 (2016).
21. E. K. H. Salje, Ferroelasticity. *Contemporary Physics* **41**, 79-91 (2000).
22. J. Sapriel, Domain-wall orientations in ferroelastics. *Physical Review B* **12**, 5128-5140 (1975).
23. K. Aizu, Possible Species of Ferromagnetic, Ferroelectric, and Ferroelastic Crystals. *Physical Review B* **2**, 754-772 (1970).
24. K. Aizu, Possible Species of "Ferroelastic" Crystals and of Simultaneously Ferroelectric and Ferroelastic Crystals. *Journal of the Physical Society of Japan* **27**, 387-396 (1969).
25. Z. Xiao, C. Bi, Y. Shao, Q. Dong, Q. Wang, Y. Yuan, C. Wang, Y. Gao, J. Huang, Efficient, High Yield Perovskite Photovoltaic Devices Grown by Interdiffusion of Solution-Processed Precursor Stacking Layers. *Energy & Environmental Science* **7**, 2619-2623 (2014).
26. Y. H. Deng, E. Peng, Y. C. Shao, Z. G. Xiao, Q. F. Dong, J. S. Huang, Scalable fabrication of efficient organolead trihalide perovskite solar cells with doctor-bladed active layers. *Energy & Environmental Science* **8**, 1544-1550 (2015).
27. M. I. Saidaminov, A. L. Abdelhady, B. Murali, E. Alarousu, V. M. Burlakov, W. Peng, I. Dursun, L. F. Wang, Y. He, G. Maculan, A. Goriely, T. Wu, O. F. Mohammed, O. M. Bakr, High-quality bulk hybrid perovskite single crystals within minutes by inverse temperature crystallization. *Nature Communications* **6**, (2015).
28. W. Cao, G. R. Barsch, Landau-Ginzburg model of interphase boundaries in improper ferroelastic Perovskites of  $D^{184h}$  symmetry. *Physical Review B* **41**, 4334-4348 (1990).
29. L. D. Landau, E. M. Lifshits. (Oxford: Butterworth-Heinemann, 1984), vol. 8.
30. A. Tselev, E. Strelcov, I. A. Luk'yanchuk, J. D. Budai, J. Z. Tischler, I. N. Ivanov, K. Jones, R. Proksch, S. V. Kalinin, A. Kolmakov, Interplay between Ferroelastic and Metal-Insulator Phase Transitions in Strained Quasi-Two-Dimensional  $\text{VO}_2$  Nanoplatelets. *Nano Letters* **10**, 2003-2011 (2010).
31. E. K. H. Salje, *Phase transitions in ferroelastic and co-elastic crystals*. (Cambridge University Press, Cambridge, UK, ed. Student edition, 1993), pp. 230.
32. M. Honig, J. A. Sulpizio, J. Drori, A. Joshua, E. Zeldov, S. Ilani, Local electrostatic imaging of striped domain order in  $\text{LaAlO}_3/\text{SrTiO}_3$ . *Nature Materials* **12**, 1112-1118 (2013).
33. W. Schranz, P. Sonderegeld, A. V. Kityk, E. K. H. Salje, Dynamic elastic response of  $\text{KMn}_{1-x}\text{Ca}_x\text{F}_3$ : Elastic softening and domain freezing. *Physical Review B* **80**, (2009).
34. E. Soergel, Piezoresponse force microscopy (PFM). *Journal of Physics D-Applied Physics* **44**, (2011).
35. D. Denning, J. Guyonnet, B. J. Rodriguez, Applications of piezoresponse force microscopy in materials research: from inorganic ferroelectrics to biopiezoelectrics and beyond. *International Materials Reviews* **61**, 46-70 (2016).

36. A. Dazzi, R. Prazeres, E. Glotin, J. M. Ortega, Local infrared microspectroscopy with subwavelength spatial resolution with an atomic force microscope tip used as a photothermal sensor. *Optics Letters* **30**, 2388-2390 (2005).
37. A. Centrone, Infrared imaging and spectroscopy beyond the diffraction limit. *Annual review of analytical chemistry* **8**, 101-126 (2015).
38. A. M. Katzenmeyer, J. Canivet, G. Holland, D. Farrusseng, A. Centrone, Assessing chemical heterogeneity at the nanoscale in mixed-ligand metal-organic frameworks with the PTIR technique. *Angewandte Chemie* **53**, 2852-2856 (2014).
39. Y. Yuan, J. Chae, Y. Shao, Q. Wang, Z. Xiao, A. Centrone, J. Huang, Photovoltaic switching mechanism in lateral structure hybrid perovskite solar cells. *Adv. Energy Mater.* **5**, 1500615 (2015).
40. A. M. Katzenmeyer, V. Aksyuk, A. Centrone, Nanoscale infrared spectroscopy: improving the spectral range of the photothermal induced resonance technique. *Analytical Chemistry* **85**, 1972-1979 (2013).
41. F. Tang, P. Bao, Z. Su, Analysis of Nanodomain Composition in High-Impact Polypropylene by Atomic Force Microscopy-Infrared. *Analytical Chemistry* **88**, 4926-4930 (2016).
42. C. Marcott, M. Lo, K. Kjoller, C. Prater, I. Noda, Spatial differentiation of sub-micrometer domains in a poly(hydroxyalkanoate) copolymer using instrumentation that combines atomic force microscopy (AFM) and infrared (IR) spectroscopy. *Applied Spectroscopy* **65**, 1145-1150 (2011).
43. F. S. Ruggeri, G. Longo, S. Faggiano, E. Lipiec, A. Pastore, G. Dietler, Infrared nanospectroscopy characterization of oligomeric and fibrillar aggregates during amyloid formation. *Nat Commun* **6**, 7831 (2015).
44. L. Gong, D. B. Chase, I. Noda, J. L. Liu, D. C. Martin, C. Y. Ni, J. F. Rabolt, Discovery of beta-Form Crystal Structure in Electrospun Poly (R)-3-hydroxybutyrate-co-(R)-3-hydroxyhexanoate (PHBHx) Nanofibers: From Fiber Mats to Single Fibers. *Macromolecules* **48**, 6197-6205 (2015).
45. A. M. Katzenmeyer, G. Holland, K. Kjoller, A. Centrone, Absorption spectroscopy and imaging from the visible through mid-infrared with 20 nm resolution. *Analytical Chemistry* **87**, 3154-3159 (2015).
46. J. Chae, Q. F. Dong, J. S. Huang, A. Centrone, Chloride Incorporation Process in  $\text{CH}_3\text{NH}_3\text{PbI}_{3-x}\text{Cl}_x$  Perovskites via Nanoscale Bandgap Maps. *Nano Letters* **15**, 8114-8121 (2015).
47. B. Lahiri, G. Holland, A. Centrone, Chemical imaging beyond the diffraction limit: experimental validation of the PTIR technique. *Small* **9**, 439-445 (2013).
48. A. Dazzi, F. Glotin, R. Carminati, Theory of infrared nanospectroscopy by photothermal induced resonance. *Journal of Applied Physics* **107**, 124519 (2010).
49. R. Dong, Y. Fang, J. Chae, J. Dai, Z. Xiao, Q. Dong, Y. Yuan, A. Centrone, X. C. Zeng, J. Huang, High-gain and low-driving-voltage photodetectors based on organolead triiodide perovskites. *Advanced materials* **27**, 1912-1918 (2015).
50. E. Mosconi, C. Quarti, T. Ivanovska, G. Ruani, F. De Angelis, Structural and electronic properties of organo-halide lead perovskites: a combined IR-spectroscopy and ab initio molecular dynamics investigation. *Physical Chemistry Chemical Physics* **16**, 16137-16144 (2014).

51. T. J. Jacobsson, L. J. Schwan, M. Ottosson, A. Hagfeldt, T. Edvinsson, Determination of Thermal Expansion Coefficients and Locating the Temperature-Induced Phase Transition in Methylammonium Lead Perovskites Using X-ray Diffraction. *Inorganic Chemistry* **54**, 10678-10685 (2015).
52. Q. Dong, Y. Yuan, Y. Shao, Y. Fang, Q. Wang, J. Huang, Abnormal crystal growth in  $\text{CH}_3\text{NH}_3\text{PbI}_{3-x}\text{Cl}_x$  using a multi-cycle solution coating process. *Energy & Environmental Science* **8**, 2464-2470 (2015).
53. B. J. Rodriguez, C. Callahan, S. V. Kalinin, R. Proksch, Dual-frequency resonance-tracking atomic force microscopy. *Nanotechnology* **18**, (2007).
54. S. Jesse, A. P. Baddorf, S. V. Kalinin, Switching spectroscopy piezoresponse force microscopy of ferroelectric materials. *Applied Physics Letters* **88**, (2006).

### **Acknowledgments**

**Funding:** ES, JC acknowledge support under the Cooperative Research Agreement between the University of Maryland and the National Institute of Standards and Technology Center for Nanoscale Science and Technology, Award 70NANB10H193, through the University of Maryland. JH and AG thank the support from National Science Foundation under awards DMR-1505535 and DMR-1420645.

### **Author contributions:**

ES, QD, TL, and JC contributed to the project equally. ES performed optical characterization experiments, prepared figure 1, 2 and wrote the related part of the manuscript. QD, YS and YD prepared the thin film and single crystal perovskite samples. TL performed PFM measurements and prepared Figure 3, 4, S1 and S2. JC performed PTIR measurements. AC and JC prepared figures 5, S3, S4. AG, JH and AC have supervised the project and wrote the PFM, sample preparation and PTIR sections of the manuscript, respectively. All of the authors discussed the results and commented on the manuscript.

### **Competing interests:**

The authors declare that they have no competing interests.

### **Data and materials availability:**

All data needed to evaluate the conclusions in the paper are present in the paper and/or the Supplementary Materials. Additional data available from authors on request.

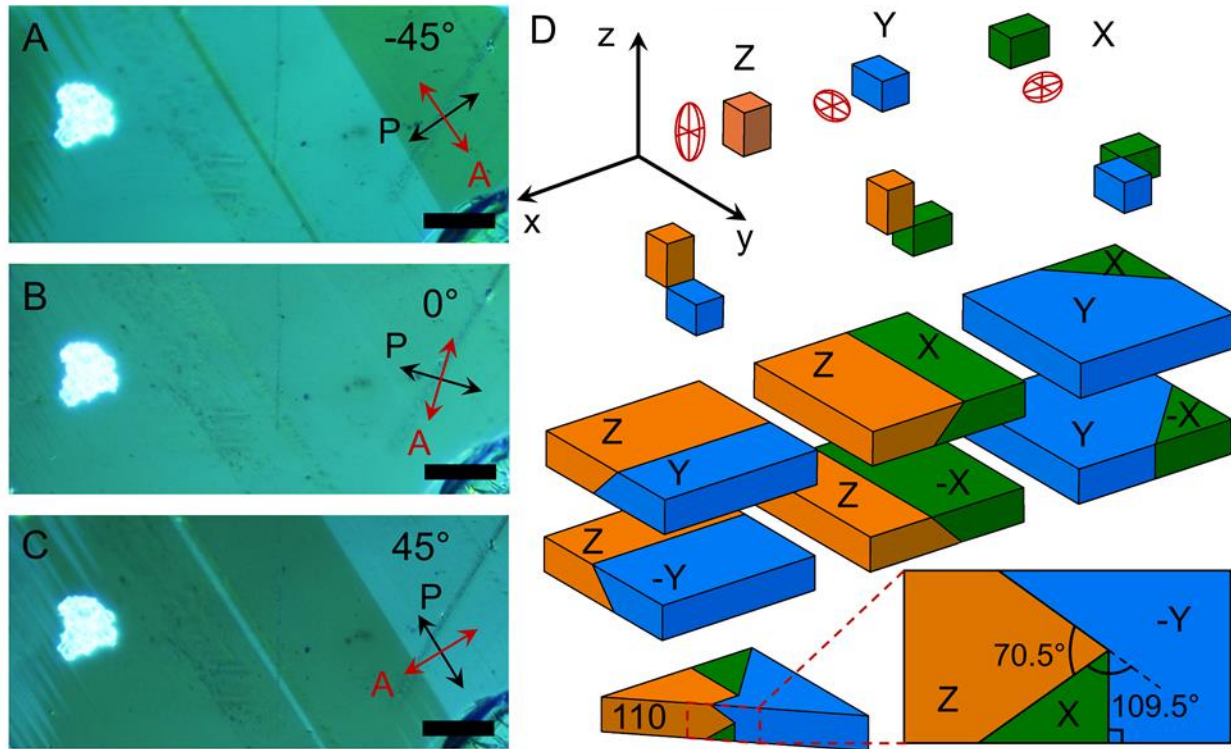


**Fig. 1. Polarized light optical images and domain configurations in MAPbI<sub>3</sub> single crystal (Sample C).** (A to C) Reflection mode polarized optical micrographs (crossed Nicols) showing contrast reversal of domain groups as a function of sample rotation relative to the polarizer-analyzer (P-A) pair. At 0° relative angle the domain groups are indistinguishable, and at 45° and -45° the domain contrast is maximum; i.e.  $\theta_e = 90^\circ$ . The red and black arrows indicate the P-A orientation, respectively. The light intensity of a bright dust particle is insensitive to the sample rotation. The scale bar is 5  $\mu\text{m}$  in all panels. (D) Permissible domains of the MAPbI<sub>3</sub> tetrahedral phase. At the cubic to tetrahedral transition, the tetrahedral unit cell can form with the c-axis aligned along any of the 3 axes (x, y, z) of the parental cubic phase, leading to 3 possible configurations (X, Y, Z). To preserve crystal integrity, the a-axes of different

domains must coincide, (32) leading to 6 possible domain orientations that are characterized by domain walls intercepting at  $0^\circ$ ,  $90^\circ$  or  $45^\circ$  in the principal plains of the parental phase, and at  $\approx 70^\circ$  and  $\approx 110^\circ$  in the (110) plane.

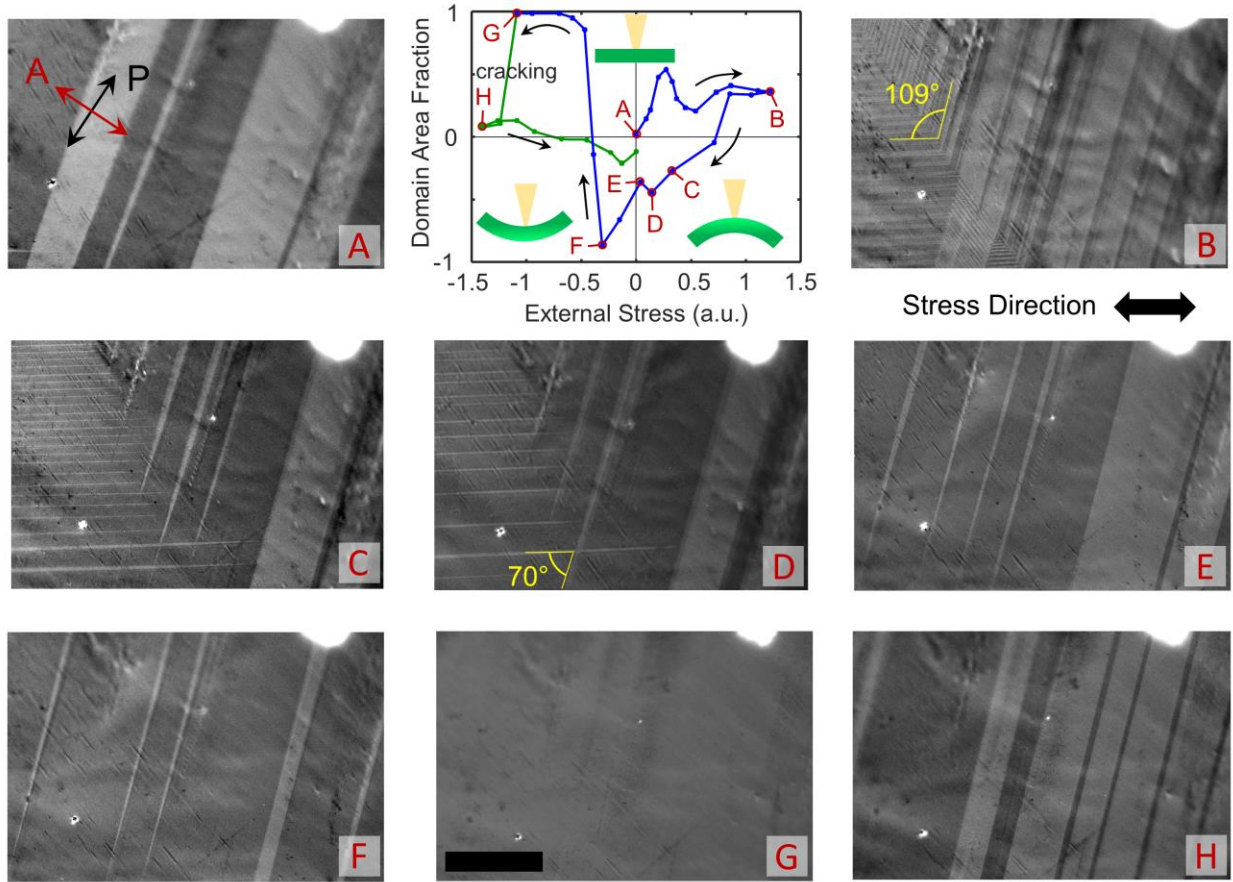


**Fig. 2. Evolution of the domain structure in *Sample C* under external stress.** Domain area fraction ( $F$ ) vs. applied uniaxial stress graph and polarized light micrograph images corresponding to letter labels. Arrows indicate the sequence of the applied stress throughout the experiment. Panels A through H correspond to selected points on the graph. Application of tensile stress (positive) leads to shifts of domain boundaries and formation of new types of domains (titled  $70^\circ$  and  $109^\circ$  to the old domains). A prominent non-linearity is observed. Compressive stress eventually erases all domains, and after point G

(where only one bright domain exists in the field of view) leads to fracturing (cracking) of the crystal and to a drastic change in the domain structure. Datapoints following cracking are marked in green color. Uncertainty in the  $F$  values was estimated to be  $\approx 0.03$ , taken as the largest of the uncertainties calculated from selected points in the graph (see methods for details) Scale bar is  $10\ \mu\text{m}$  for all panels. The domain area fraction was calculated for a field of view larger than shown ( $530\ \mu\text{m} \times 710\ \mu\text{m}$ ). Micrographs were grayscale. The graph insets show schematics of sample bending relative to the incident light (yellow cone).

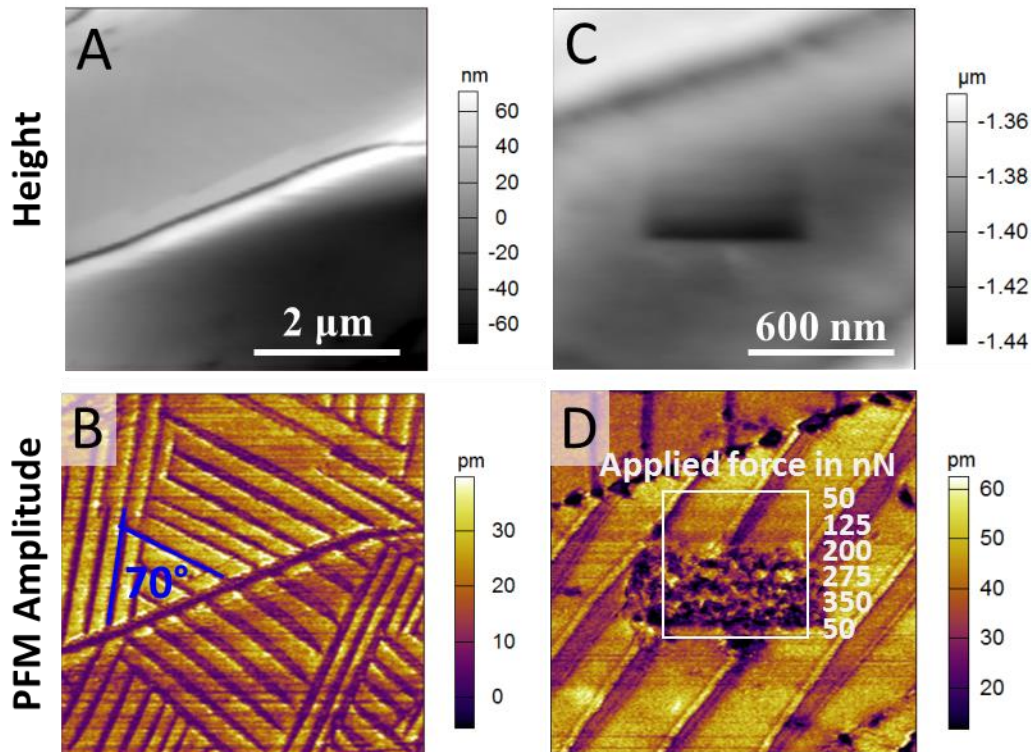


**Fig. 3. Observation of ferroelastic domain pattern by PFM.** (A and B) Topography and PFM amplitude images of *Sample B1* (fabricated by doctor-blade coating) showing different-orientated ferroelastic domain. (C and D) High resolution topography and PFM amplitude images of *Sample B1* showing that the application of a localized load by the AFM tip does not change the stripes long range characteristics.

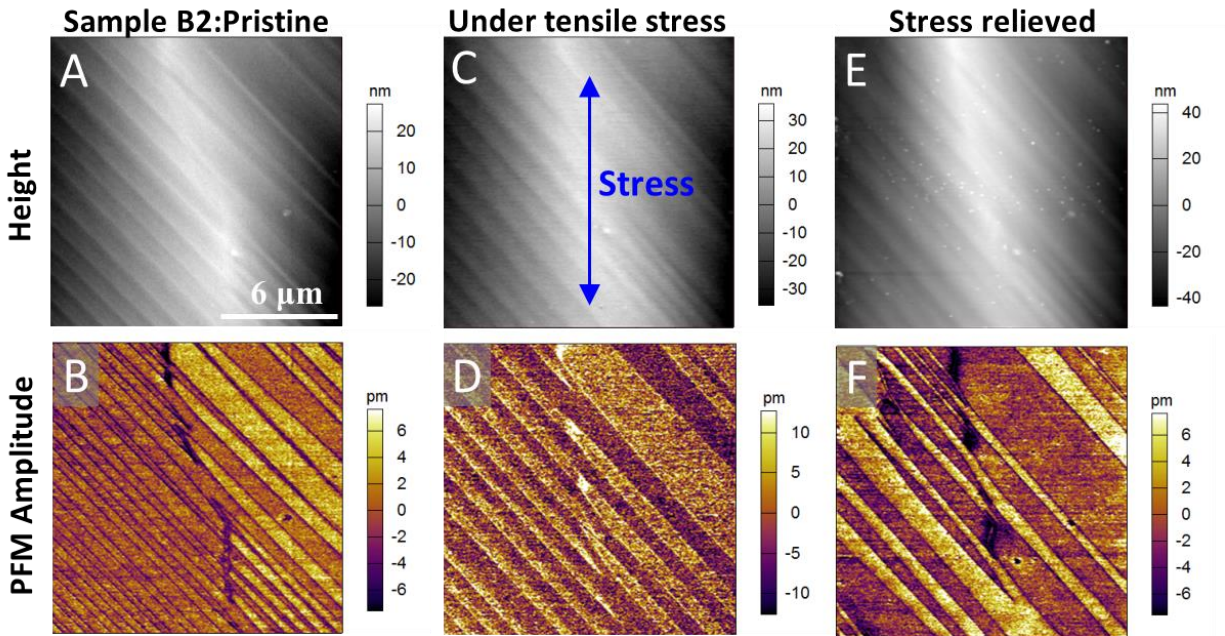


**Fig. 4. PFM observation of ferroelastic domain pattern modulated by external stress.** Topography and PFM amplitude images of *Sample B2* (fabricated by doctor-blade coating): in pristine state (**A** and **B**), under tensile stress (**C** and **D**), and after relieving the stress (**E** and **F**). The blue arrows in (**C**) indicate the direction of the applied stress.

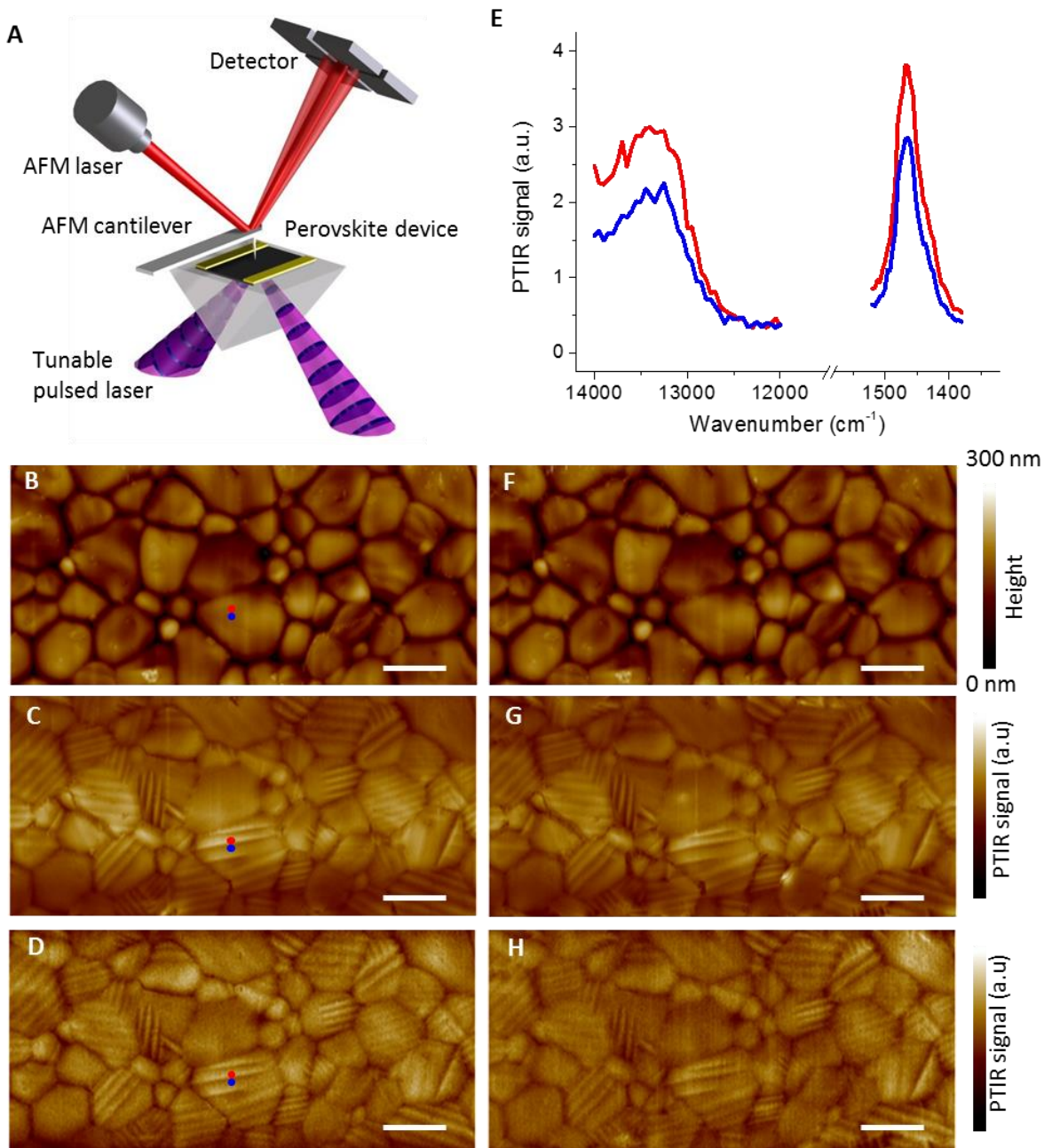


**Fig. 5. Observation of ferroelastic domains by PTIR in and their insensitivity to the applied electric field.** (A) Schematic illustration of the PTIR measurement: an AFM cantilever measures the thermal expansion resulting from light absorption. (B) AFM topography image of the *Sample A2* area between electrodes and corresponding PTIR images of (C) CH<sub>3</sub> asymmetric deformation of the methyl ammonium ion (1468 cm<sup>-1</sup>) and (D) electronic transition above bandgap (13250 cm<sup>-1</sup>, 1.64 eV) of the as prepared sample. (E) Representative electronic (left side) and vibrational (right side) absorption spectra obtained

from contiguous bright (red dot) and dark (blue dot) striations visible in PTIR images. (F) *Sample A2* AFM topography image and corresponding PTIR images at  $1468\text{ cm}^{-1}$  (G) and  $13250\text{ cm}^{-1}$  (H) obtained after applying a bias of  $0.86\text{ V}\cdot\mu\text{m}^{-1}$  for 1 min (in plane electric field). All scale bars are  $2\ \mu\text{m}$ .

## Supplementary Materials

### **CH<sub>3</sub>NH<sub>3</sub>PbI<sub>3</sub> Perovskites: Ferroelasticity Revealed**

Evgheni Strelcov,<sup>1,2†</sup> Qingfeng Dong,<sup>3†</sup> Tao Li,<sup>4†</sup> Jungseok Chae,<sup>1,2†</sup> Yuchuan Shao,<sup>3,4</sup> Yehao Deng,<sup>3,4</sup> Alexei Gruveman,<sup>4\*</sup> Jinsong Huang,<sup>3\*</sup> and Andrea Centrone<sup>1\*</sup>

† These authors contributed equally to this work

\* Corresponding authors: agruverman2@unl.edu, jhuang2@unl.edu, andrea.centrone@nist.gov

<sup>1</sup> Center for Nanoscale Science and Technology, National Institute of Standards and Technology  
100 Bureau Drive, Gaithersburg, MD 20899, USA.

<sup>2</sup> Maryland Nanocenter, University of Maryland, College Park, MD 20742 USA.

<sup>3</sup> Department of Mechanical and Materials Engineering, University of Nebraska-Lincoln,  
Lincoln, Nebraska 68588, USA.

<sup>4</sup> Department of Physics and Astronomy, University of Nebraska-Lincoln, Lincoln, Nebraska  
68588, USA

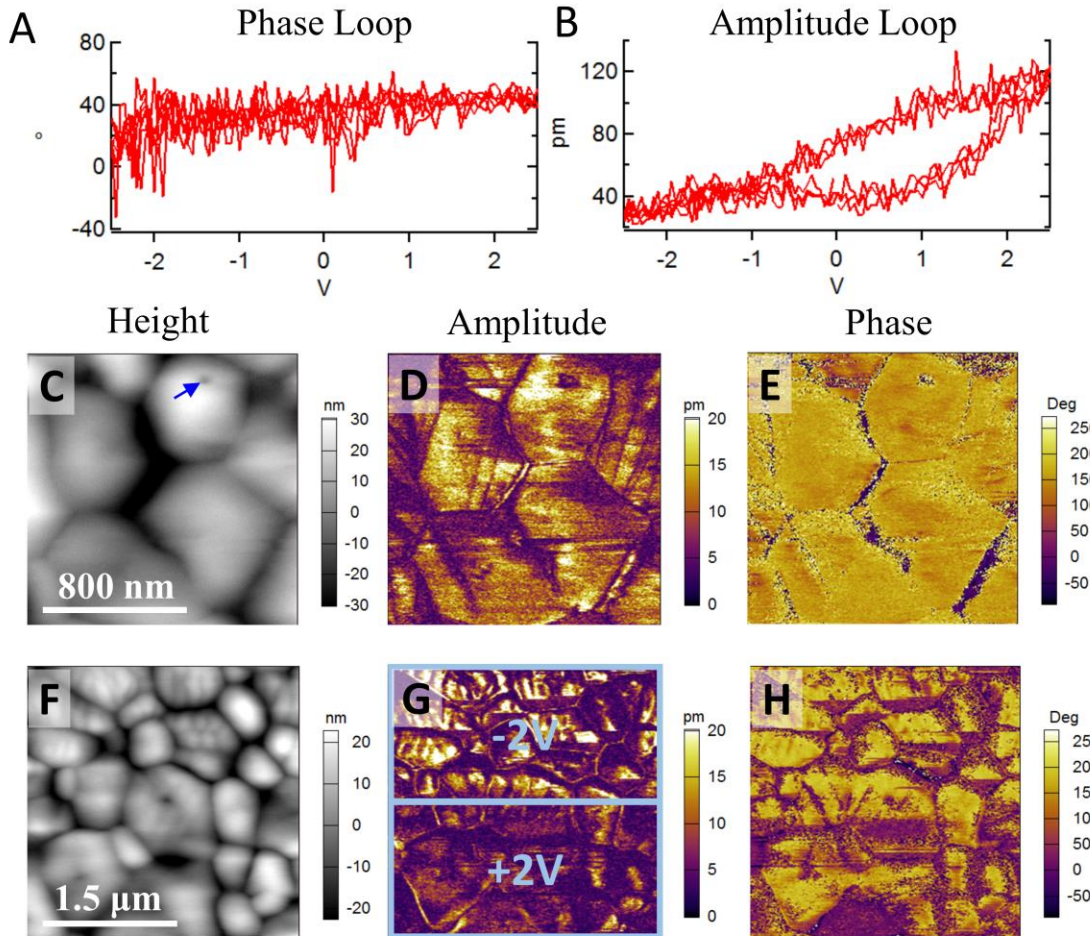
## List of Supplementary Materials

Fig. S1. Piezoresponse Force Microscopy measurements on Sample A1 do not show evidence of ferroelectric behavior.

Fig. S2. Representative PFM images showing strong amplitude contrast and very weak phase contrast.

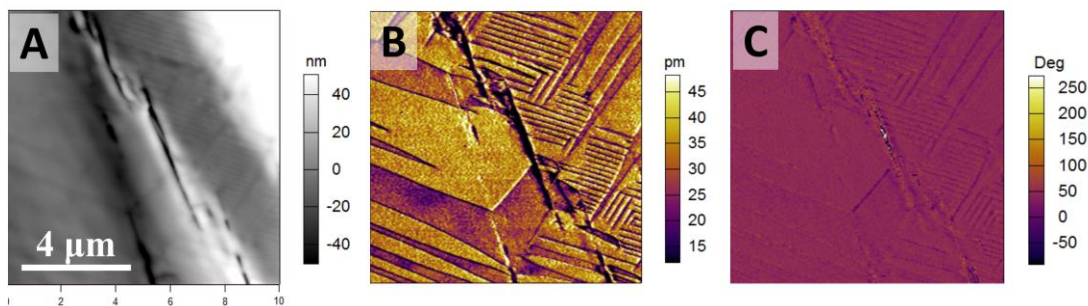
Fig. S3. Observation of ferroelastic domains by PTIR.

Fig. S4. Observation of ferroelastic domains by PTIR with s- and p-light polarization.



**Fig. S1. Piezoresponse Force Microscopy measurements on *Sample A1* do not show evidence of ferroelectric behavior.** (A and B) phase and amplitude hysteresis loops measured in the location indicated by the blue arrow in panel (C) by applying voltage locally with the PFM tip. The constant value of phase loop indicates no polarization switching occurred i.e. no ferroelectric behavior is detected. The applied DC electric bias only cause redistribution of charged carriers that produces the asymmetric electromechanical strain under positive and negative biases as seen in the amplitude loop. Because the  $\pm 2.5$  V applied bias has caused local degradation of the film in the position indicated by the arrow, the DC bias applied to sample for the subsequent measurements was always kept below 2.5 V. (C to E) Topography and PFM amplitude and phase images after the hysteresis measurement. (F to H) Topography and PFM amplitude and phase images obtained after poling the sample with -2V (top half images) and + 2 V (bottom half

images) DC bias applied to the sample via scanning using the biased PFM tip. There is no clear contrast between the regions poled by positive and negative biases.



**Figure. S2. Representative PFM images showing strong amplitude contrast and very weak phase contrast.** (A to C) Topography (A) and corresponding amplitude (B) and phase (C) images of in *Sample B1*. Strong amplitude contrast and very weak phase contrast indicate absence of ferroelectric domains in the  $\text{MAPbI}_3$  films.

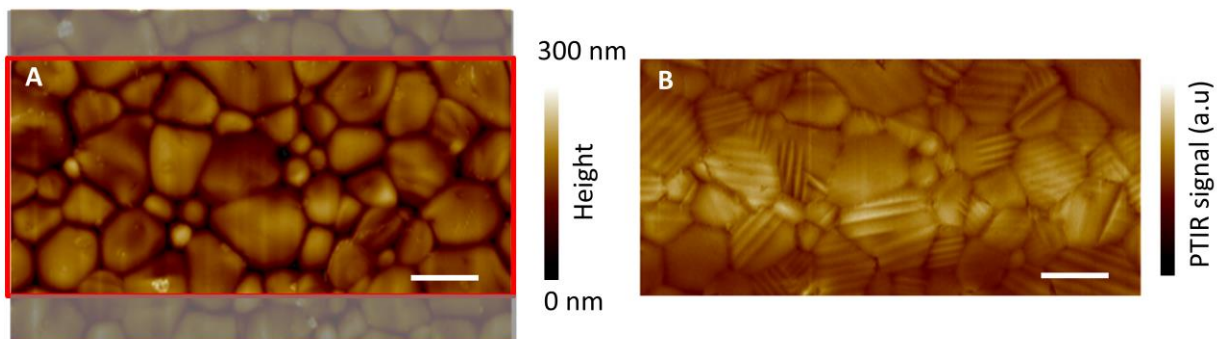


**Fig. S3. Observation of ferroelastic domains by PTIR.** (A) *Sample A2* AFM topography image showing  $\text{MAPbI}_3$  in between the electrodes (red box) and the  $\text{MAPbI}_3$  covered electrodes (semitransparent gray areas). The red box defines the same area illustrated in figure 4 of the main text. (B) PTIR image of  $\text{CH}_3$  asymmetric deformation of the methyl ammonium ion ( $1468 \text{ cm}^{-1}$ ) of the area defined by the red box in panel a (Same image in Fig. 4) box in a. (The same image as shown in Fig. 4C. All scale bars are  $2 \mu\text{m}$ ).

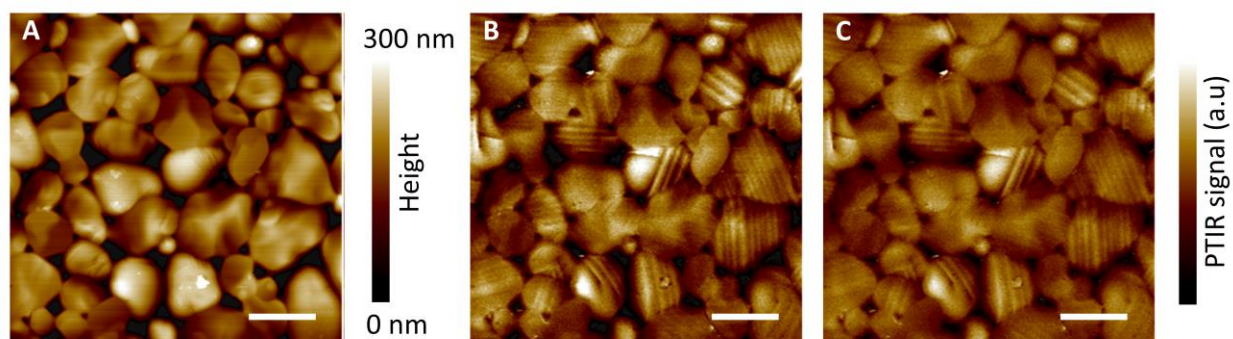


**Fig. S4. Observation of ferroelastic domains by PTIR with *s*- and *p*-light polarization.** (A) AFM topography image of the *Sample A2* (area away from the electrodes) and corresponding PTIR absorption maps recorded by illuminating the sample at  $1468\text{ cm}^{-1}$  ( $\text{CH}_3$  asymmetric deformation of the methyl ammonium ion) with (B) *s*-polarized light (light polarization in the sample plane), and (C) with *p*-polarized (light polarization with components in the sample plane and out of plane). All scale bars are  $3.0\text{ }\mu\text{m}$ .